JOURNAL OF SOLID STATE CHEMISTRY 114, 15–23 (1995)

Synthesis, Crystal Structure, and Electrical Properties of the Pyrochlores $Pb_{2-x}Ln_xRu_2O_{7-y}$ (Ln = Nd, Gd)

H. Kobayashi, R. Kanno,[1] and Y. Kawamoto

Department of Chemistry, Faculty of Science, Kobe University, Nada, Kobe, Hyogo, 657 Japan

T. Kamiyama

Institute of Materials Science, University of Tsukuba, Tennodai, Tsukuba, Ibaraki, 305 Japan

F. Izumi

National Institute for Research in Inorganic Materials, 1-1, Namiki, Tsukuba, Ibaraki, 305 Japan

and

A. W. Sleight

Department of Chemistry, Oregon State University, Corvallis, Oregon

Received November 1, 1993; in revised form March 3, 1994; accepted March 4, 1994

The lead–lanthanoid pyrochlores $Pb_{2-x}Ln_xRu_2O_{7-y}$ (Ln = Nd, Gd) have been synthesized and characterized by X-ray diffraction, neutron diffraction, and electrical resistivity measurements. The solid solutions synthesized from metal nitrates and ruthenium oxide showed two monophasic regions in both neodymium and gadolinium systems: an oxygen-vacancy-ordered phase with $F\bar{4}3m$ symmetry for the lead-rich region, $0 \le x \le 0.2$, and a vacancy-disordered phase with $Fd\bar{3}m$ symmetry for the lanthanoid-rich region, $1.0 \le x \le 2.0$. Electrical resistivity measurements showed a metallic behavior for the lead-rich region of the solid solutions ($0 \le x \le 0.2$). In the lanthanoid-rich region, a change from metallic to semiconducting behavior was observed at $1.0 < x < 1.2$ and $1.2 < x < 1.5$ in $Pb_{2-x}Nd_xRu_2O_{7-y}$ and $Pb_{2-x}Gd_xRu_2O_{7-y}$, respectively. From x = 1.0 to 2.0, the lattice parameters increase in $Pb_{2-x}Nd_xRu_2O_{7-y}$ and decrease in $Pb_{2-x}Gd_xRu_2O_{7-y}$. However, Rietveld analysis of $Pb_{2-x}Ln_xRu_2O_{7-y}$ at room temperature indicates similar structural changes in both systems; the Ru–O(1) bond length decreases and the bend in RuO_6 zigzag chains increases with increasing x. The analysis of neutron diffraction data for $PbNdRu_2O_{7-y}$ indicates the existence of oxygen vacancies, y = 0.188(8), with no evidence for long-range ordering. The relationship between the structural changes and the electrical properties is discussed.

INTRODUCTION

The pyrochlores $A_2Ru_2O_7$ exhibit a wide range of electrical resistivities: $Bi_2Ru_2O_7$ and $Pb_2Ru_2O_{6.5}$ are metallic and Pauli paramagnetic with low resistivities of $10^{-3}\ \Omega \cdot$ cm at room temperature; $Ln_2Ru_2O_7$ (Ln = Pr–Lu) and $Y_2Ru_2O_7$ are semiconducting with low activation energies (1–4); and $Tl_2Ru_2O_{7-y}$ shows a metallic–semiconducting transition around 120 K (5). To understand their high electrical conductivities, the electronic structures of $Bi_2Ru_2O_7$, $Y_2Ru_2O_7$, and $Pb_2Ru_2O_{6.5}$ have recently been investigated by XPS, UPS, and HREELS (6–8) and by the pseudofunction method (9). The unoccupied Pb or Bi 6p states are close to E_F and contribute to metallic conductivity by mixing with Ru 4d state via the framework oxygen.

The relationship between the electrical properties and the crystal structures has recently been reported by Kanno *et al.* (10) and Yamamoto *et al.* (11) for the solid solutions, $Bi_{2-x}Ln_xRu_2O_7$ (Ln = Y, Pr–Lu). The metallic-to-semiconducting change is related to their structural changes determined by X-ray Rietveld analysis as follows: (i) the Ru–O(1) bondlength in the RuO_6 octahedra increases, (ii) the distortion of the RuO_6 octahedra increases, and (iii) the bend in the RuO_6 zigzag chains increases with increasing Ln^{3+} contents. The structural analysis using X-ray Rietveld refinement provided a convenient and powerful probe into the structural variations of the pyrochlore solid solutions.

The solid solutions based on the lead–ruthenium pyrochlores have been synthesized by the alkaline medium method, which allowed substitution of up to 50% of the Pb ions on the B site (12). Resistivity vs temperature data for the solid solutions $Pb_2[Pb_xRu_{2-x}]O_{7-y}$ showed a

[1] To whom correspondence should be addressed.

0022-4596/95 $6.00

smooth change from a positive to a negative temperature coefficient of resistivity as a function of increasing lead content. However, no solid solution formation has been reported for the substitution on the A site by lanthanoid ions.

The crystal structure of the lead–ruthenium pyrochlore has been determined by Beyerlein *et al.* (13). Their neutron diffraction study confirmed half occupancy of the O′ site, leading to the chemical formula $Pb_2Ru_2O_{6.5}$. This site is half occupied and the ordering of the remaining oxygen results in a symmetry reduction from $Fd\bar{3}m$ to $F43m$, and each Pb atom in the structure was displaced by 0.040(4) Å toward its associated vacancy. Since the lead–ruthenium pyrochlore has ordered oxygen vacancies, the solid solutions with lanthanoid–ruthenium pyrochlores might give structural variations on both the A_2O network and the RuO_3 conduction network which affect their electrical properties. In the present study, the solid solutions $Pb_{2-x}Ln_xRu_2O_{7-y}$ (Ln = Nd, Gd) were synthesized and their formation ranges were determined. The electrical properties and the crystal structures of these solid solutions were determined.

EXPERIMENTAL

The solid solutions $Pb_{2-x}Ln_xRu_2O_{7-y}$ (Ln = Nd, Gd) were prepared by heating appropriate molar ratios of oxides, Nd_2O_3, Gd_2O_3, RuO_2, PbO, PbO_2, or nitrates, $Pb(NO_3)_2$, $Nd(NO_3)_3 \cdot 6H_2O$, $Gd(NO_3)_3 \cdot 6H_2O$ (RuO_2, >99.99% purity, Nd_2O_3, >99.9% purity, Furuuchi Chemicals Ltd.; PbO, >99%, and PbO_2, >97% purity, Nakarai Chemicals Ltd.; $Nd(NO_3)_3 \cdot 6H_2O$, $Gd(NO_3)_3 \cdot 6H_2O$, >99.5% purity, Wako Chemical Industries Ltd.). They were weighed, mixed under an argon atmosphere, pressed into pellets, and then calcined at 1073–1173 K for 2 days. After being reground, the samples were pressed into pellets again, and fired at 1123–1423 K for 2–6 days.

X-ray diffraction (XRD) patterns of powdered samples were obtained with a high-power X-ray powder diffractometer (Rigaku RAD-C, 12 kW). A curved graphite monochromator equipped after the sample position was used for lowering the background. Diffraction data were collected with Cu$K\alpha$ radiation for 3 sec at each 0.04° stepwidth over a 2θ range from 10 to 105° at room temperature. Structural parameters were refined by Rietveld analysis with the computer program RIETAN (14). Reflection positions and intensities were calculated for both Cu$K\alpha_1$ and Cu$K\alpha_2$ with a factor of 0.5 applied to the calculated integrated intensities of Cu$K\alpha_2$ peaks. A pseudo-Voigt profile-shape function was used; the mixing parameter γ was included in the least-squares refinements. The 420 reflection which is indicative of oxygen-vacancy ordering was measured by step scanning with a step width of 0.02° and a counting time of 90 sec.

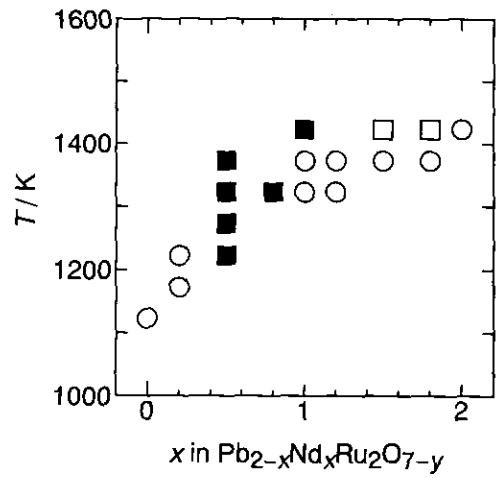

FIG. 1. Formation diagram of $Pb_{2-x}Nd_xRu_2O_{7-y}$: (○), single-phase of the pyrochlore; (■), two pyrochlore phases with different lattice parameters; (□), two phases with the pyrochlore and Nd_3RuO_7.

Neutron diffraction data were taken on a time-of-flight (TOF) neutron powder diffractometer, HRP (15), at the KENS pulsed spallation neutron source at the National Laboratory High Energy Physics (KEK). The specimen was contained in a cylindrical vanadium cell of dimensions 5 mm in radius, 55 mm in height, and 200 μm in thickness. The average scattering angle, 2θ, was fixed at 170°, and intensity data were collected at 300 K.

The electrical resistivity was measured for the sintered materials with dimensions of approximately 2 × 2 × 5 mm. The data were obtained by the dc four-probe method with silver-paste contact in the temperature range $15 \leq T \leq 300$ K using a Toyo–Sanso low-temperature electrical-conductivity measurement unit. The temperature of the samples was measured using a Au + 0.07% Fe–chromel thermocouple.

RESULTS AND DISCUSSION

Synthesis

(*a*) *$Pb_{2-x}Nd_xRu_2O_{7-y}$.* The quaternary oxides, $Pb_{2-x}Nd_xRu_2O_{7-y}$, were prepared by heating mixtures of PbO, Nd_2O_3, and RuO_2 in air at temperatures between 1123 and 1423 K. However, impurity phases such as RuO_2 and Nd_3RuO_7 (16) were observed in the whole composition range. The solid solutions were therefore synthesized using more reactive starting materials, $Pb(NO_3)_2$, $Nd(NO_3)_3 \cdot 6H_2O$, and RuO_2. They were mixed, pelletized, and heated at 1123–1423 K for 4 days, followed by successive firing at 1173 K and regrindings. Figure 1 shows the formation diagram of $Pb_{2-x}Nd_xRu_2O_{7-y}$. Monophasic properties of the pyrochlore structure were observed for $0.0 \leq x \leq 0.2$ and $1.0 \leq x \leq 2.0$ in $Pb_{2-x}Nd_xRu_2O_{7-y}$.

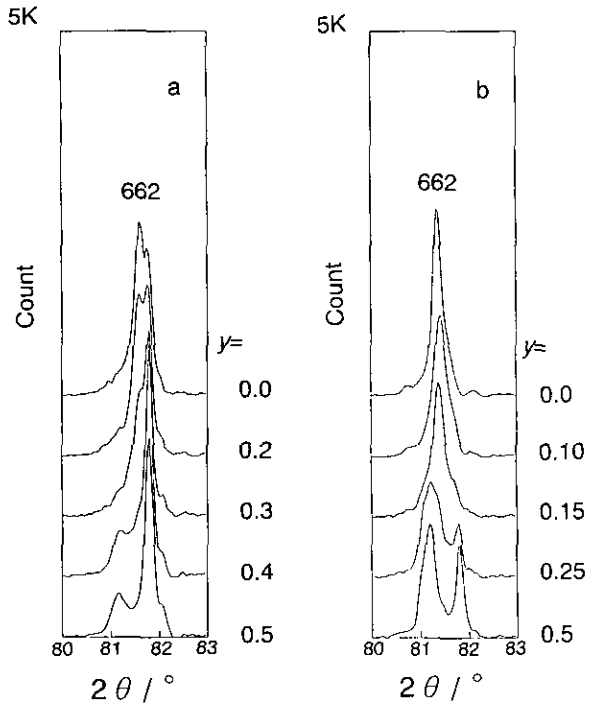

FIG. 2. XRD patterns for (a) $Pb_{1.5}Nd_{0.5}Ru_2O_{7-y}$ and (b) $PbNdRu_2O_{7-y}$ as a function of oxygen content, y.

Two pyrochlore phases with different lattice parameters were observed for the samples at $x = 0.5$ and 0.8. We tried to synthesize the monophasic samples at the composition, $x = 0.5$, under controlled oxygen partial pressure. The oxygen contents of the reactants were fixed from $y = 0.0$ to 0.5 in $Pb_{1.5}Nd_{0.5}Ru_2O_{7-y}$ with a changing PbO/PbO_2 ratio. The starting materials, PbO, PbO_2, Nd_2O_3, and RuO_2 were mixed, pelletized, sealed in an evacuated quartz tube, and heated at 1223 K for 3 days. Figure 2a shows the XRD patterns around the 662 reflection as a function of oxygen content, y. The 662 reflections split into two at all compositions synthesized in the present study. These results indicate that the whole range of solid solutions was not obtained for the $Pb_{2-x}Nd_xRu_2O_{7-y}$ system.

The neodymium pyrochlore, $Nd_2Ru_2O_7$, has been reported to have cubic $Fd\bar{3}m$ symmetry with no oxygen vacancy (11), while in $Pb_2Ru_2O_{6.5}$, the oxygen vacancy of the amount of 0.5 ordered at the defect O′ site in the pyrochlore structure, which leads to the symmetry reduction from $Fd\bar{3}m$ to $F\bar{4}3m$ (13). The symmetry difference between the two end-members may prevent the full range formation of solid–solution.

The oxygen-vacancy ordering in the lead pyrochlore is characterized by superlattice XRD peaks, such as the 420 and 640 reflections (11). In order to clarify the oxygen-vacancy ordering in these solid solutions, the XRD measurements were carried out near the 420 superlattice reflections. Figure 3a shows the XRD patterns for $Pb_{2-x}Nd_xRu_2O_{7-y}$ as a function of composition, x. The 420 reflection is clearly observed for $x = 0.2$. Its intensity decreases with increasing x, and the peak finally disappeared around $x = 1.0$. These results indicate that (i) the lead-rich region of the solid solution ($0 \le x \le 0.2$) has $F\bar{4}3m$ symmetry with vacancy ordering, (ii) the neodymium-rich region of the solid solution ($1.0 \le x \le 2.0$) has $Fd\bar{3}m$ symmetry with no vacancy ordering, and (iii) the diphasic region ($0.5 \le x < 1.0$) is a mixture of the $Fd\bar{3}m$ and $F\bar{4}3m$ phases.

To estimate the number of oxygen vacancies in the solid solutions, we synthesized $PbNdRu_2O_{7-y}$ in a sealed, evacuated quartz tube at 1323 K for 48 hr under a controlled oxygen content of the starting materials. Figure 2b shows the XRD patterns of $PbNdRu_2O_{7-y}$ as a function of oxygen vacancy, y. The 662 peak splits into two for the sample with $y = 0.5$ in $PbNdRu_2O_{7-y}$, and this splitting becomes less with decreasing y. The monophasic properties were observed for the samples with the amount of oxygen vacancy, $y \approx 0.1$. The composition of this solid solution was therefore $PbNdRu_2O_{6.9-7.0}$ with no long-range ordering of the oxygen vacancies.

(b) $Pb_{2-x}Gd_xRu_2O_{7-y}$. The quaternary oxides, $Pb_{2-x}Gd_xRu_2O_{7-y}$, were prepared by heating mixtures of $Pb(NO_3)_2$, $Gd(NO_3)_3 \cdot 6H_2O$, and RuO_2 in air at 1123–1423 K for four days followed by subsequent heatings at 1173 K and regrindings. Monophasic properties were observed

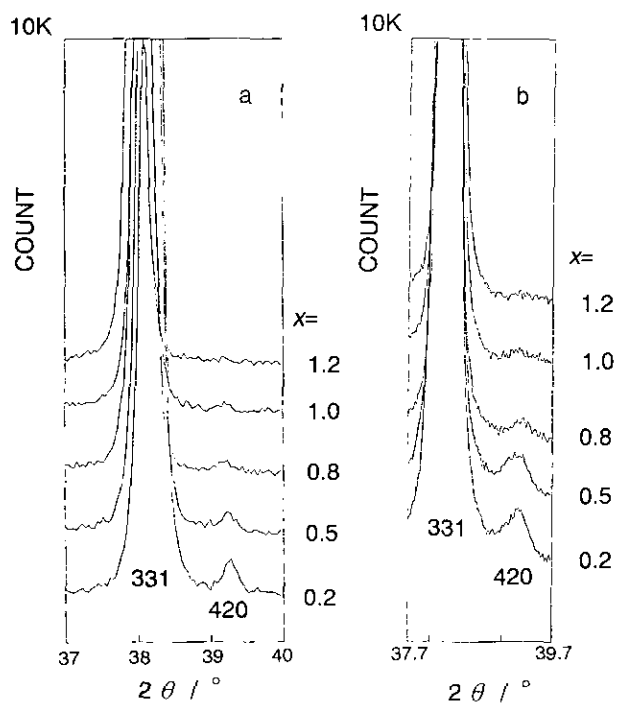

FIG. 3. XRD patterns near the 420 superlattice reflection for (a) $Pb_{2-x}Nd_xRu_2O_{7-y}$ and (b) $Pb_{2-x}Gd_xRu_2O_{7-y}$.

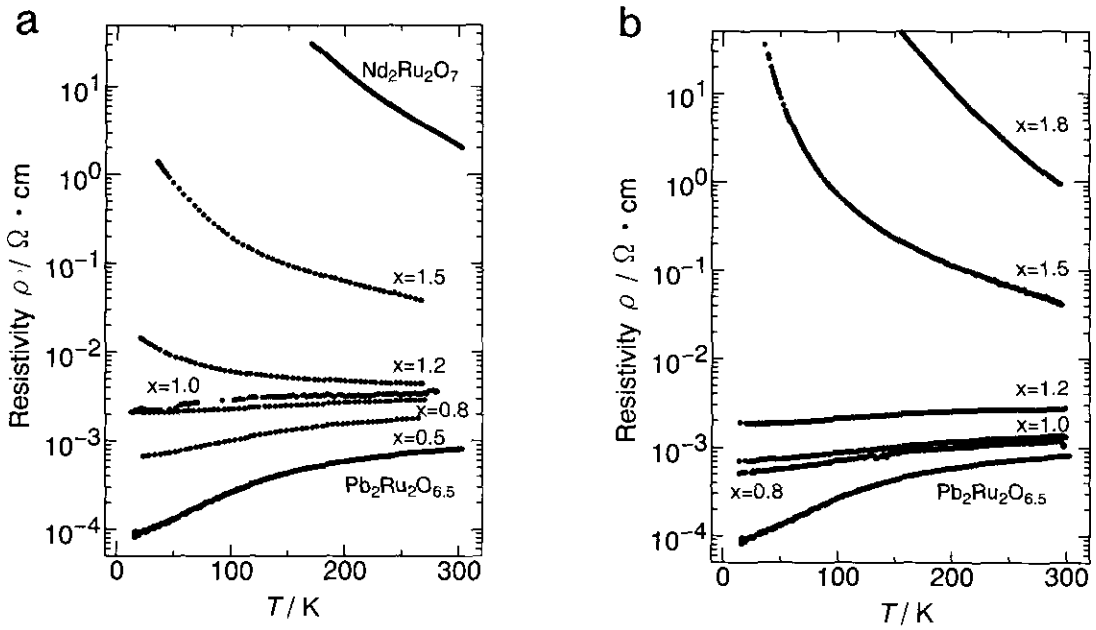

FIG. 4. Temperature dependence of the resistivity for (a) $Pb_{2-x}Nd_xRu_2O_{7-y}$ and (b) $Pb_{2-x}Gd_xRu_2O_{7-y}$.

for the whole range of solid solutions. However, the difference in lattice parameters between two end-members, $Pb_2Ru_2O_{6.5}$ and $Gd_2Ru_2O_7$, might not be large enough to establish the diphasic region. Figure 3b shows the XRD patterns for $Pb_{2-x}Gd_xRu_2O_{7-y}$ near the 420 superlattice reflection. The intensity of the 420 reflection decreased from $x = 0.5$ to 1.0, and this peak disappeared around $x = 1.0$–1.2. These changes are quite similar to those found in $Pb_{2-x}Nd_xRu_2O_{7-y}$, and suggest the existence of the diphasic region. The phase relationships in $Pb_{2-x}Gd_xRu_2O_{7-y}$ estimated from the above results are as follows: the monophasic $Fd\bar{3}m$ phase for the gadolinium-rich region of $1.0 < x \leq 2.0$ where no superlattice reflection was observed, the monophasic $F\bar{4}3m$ phase for the lead-rich region of $0 \leq x < \sim 0.5$, and the diphasic region of the $Fd\bar{3}m$ and $F\bar{4}3m$ phases for $\sim 0.5 \leq x \leq 1.0$.

Electrical Properties

Figure 4 shows the temperature dependence of the resistivity for $Pb_{2-x}Ln_xRu_2O_{7-y}$. $Pb_2Ru_2O_{6.5}$ shows metallic,

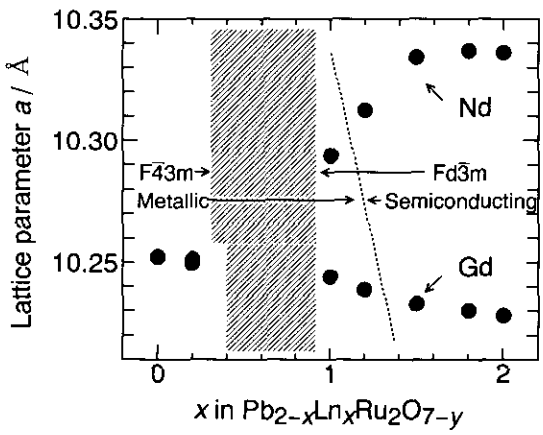

FIG. 5. Relationship among the lattice parameters, lattice symmetry, and electrical properties in the $Pb_{2-x}Ln_xRu_2O_{7-y}$ (Ln = Nd, Gd) solid solutions.

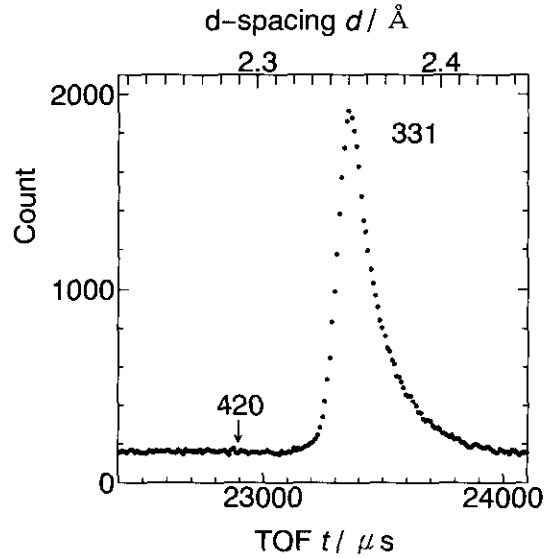

FIG. 6. Raw TOF neutron diffraction data showing the 311 reflection for $PbNdRu_2O_{7-y}$. The position of the 420 reflection is indicated.

TABLE 1
Structure Parameters for $PbNdRu_2O_{7-y}$ in $Fd\bar{3}m$

a = 10.29778(18) Å, R_{wp} = 4.59%, R_p = 3.61%, R_I = 2.49%, R_F = 1.88%, R_e = 5.05%

Atom	Site	g	x	y	z	B_{eq} (Å^2)[a]
Pb	16*d*	0.56(3)	1/2	1/2	1/2	0.79
Nd	16*d*	0.44	1/2	1/2	1/2	=*B*(Pb)
Ru	16*c*	0.962(4)	0	0	0	0.25
O(1)	48*f*	1.0	0.32510(8)	1/8	1/8	0.69
O(2)	8*b*	0.812(8)	3/8	3/8	3/8	1.46
Atom	U_{11} (Å^2)	U_{22} (Å^2)	U_{33} (Å^2)	U_{12} (Å^2)	U_{13} (Å^2)	U_{23} (Å^2)
Pb/Nd	0.0100(3)	$=U_{11}$	$=U_{11}$	0.0002(2)	$=U_{12}$	$=U_{12}$
Ru	0.0032(2)	$=U_{11}$	$=U_{11}$	−0.0005(2)	$=U_{12}$	$=U_{12}$
O(1)	0.0122(3)	0.0070(2)	$=U_{22}$	0	0	0.0022(3)
O(2)	0.0185(8)	$=U_{11}$	$=U_{11}$	0	0	0

Note. Numbers in parentheses are estimated standard deviations of the last significant digit. The form of the anisotropic temperature factor is $\exp[-2\pi^2(h^2a^{*2}U_{11} + k^2b^{*2}U_{22} + l^2c^{*2}U_{33} + 2hka^*b^*U_{12} + 2hla^*c^*U_{13} + 2klb^*c^*U_{23})]$.

[a] B_{eq}: Equivalent isotropic thermal parameter.

while $Nd_2Ru_2O_7$ and $Gd_2Ru_2O_7$ show semiconducting behavior as indicated previously (1–4). The resistivities increase with Ln^{3+} content and a change from metallic to semiconducting behavior was observed at x = 1.0–1.2 in $Pb_{2-x}Nd_xRu_2O_{7-y}$ and at x = 1.2–1.5 in $Pb_{2-x}Gd_xRu_2O_{7-y}$. Figure 5 summarizes the lattice parameters after the Rietveld refinements, phase relations, and electrical properties for $Pb_{2-x}Ln_xRu_2O_{7-y}$ (Ln = Nd, Gd). The metallic property changes to semiconducting at a composition in the lanthanoid-rich region of $Fd\bar{3}m$ symmetry. The metallic-to-semiconducting changes were previously observed for the solid solutions, $Bi_{2-x}Ln_xRu_2O_7$ (Ln = Pr–Lu, Y), at the boundary compositions of x = 1.2–1.4, which is almost the same as those observed for $Pb_{2-x}Ln_xRu_2O_{7-y}$.

TABLE 2
Interatomic Distances and Bond Angles of Pb/Nd and Ru Environments for $PbNdRu_2O_{7-y}$ Calculated from the Structure Parameters Listed in Table 1

Distances	d (Å)
Pd/Nd–O(1[i])	2.5608(8)
Pb/Nd–O(2)	2.2295
Ru–O(1[ii])	1.9779(4)
Angles	θ (°)
O(1[i])–Pb/Nd–O(1[iii])	117.026(10)
O(1[i])–Pb/Nd–O(2)	100.041(18)
O(1[i])–Pb/Nd–O(2[iv])	79.959(17)
O(1[ii])–Ru–O(1[v])	94.90(4)
O(1[ii])–Ru–O(1[vi])	85.10(4)
Ru[vii]–O(1)–Ru[viii]	133.97(6)

Note. Coordinate triplets: i) x, y + 1/2, z + 1/2; ii) x − 1/4, y − 1/4, $-z$; iii) z + 1/4, x, y + 1/4; iv) $-x$ + 1, $-y$ + 1, $-z$ + 1; v) $-z$, x − 1/4, y − 1/4; vi) z, $-x$ + 1/4, $-y$ + 1/4; vii) $-z$ + 3/4, y + 1, $-x$ + 3/4; viii) $-x$ + 1/4, $-y$ + 1/4, z.

Structure

(*a*) *Neutron diffraction measurement.* In order to clarify the vacancy ordering and the amount of vacancy in the $Fd\bar{3}m$ phase, we determined the structure of $Pb_{2-x}Nd_xRu_2O_{7-y}$ at the boundary composition of the solid solution, x = 1.0, using neutron powder diffraction. Intensity data for interplaner spacings between 0.5 and 3.2 Å were used for Rietveld analysis, but those in TOF regions, 26,800–27,000 μsec, were excluded in the refinement owing to the appearance of very weak peaks due to an unknown impurity. Figure 6 shows raw TOF neutron data showing the 331 reflection. No superlattice 420 reflection

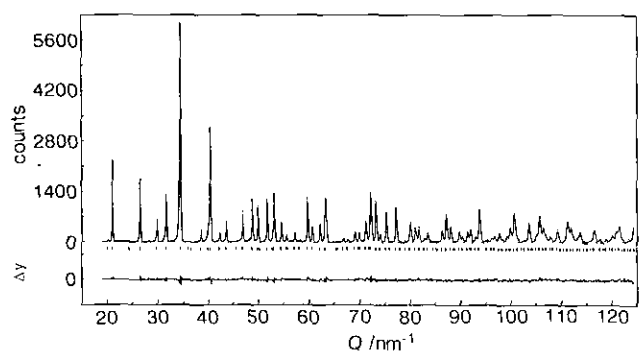

FIG. 7. Observed, calculated and difference patterns for $PbNdRu_2O_{7-y}$.

TABLE 3
Rietveld Refinement Results for $Pb_{2-x}Ln_xRu_2O_{7-y}$

			$Pb_{2-x}Nd_xRu_2O_{7-y}$		
Ln content, *x*	1.0	1.2	1.5	1.8	2.0
a (Å)	10.29367(15)	10.3125(2)	10.3343(2)	10.33705(16)	10.3362(2)
x(O1)	0.320(3)	0.322(3)	0.324(4)	0.326(4)	0.328(4)
B(Pb/Nd) (Å^2)	0.81(13)	0.41(10)	0.40(13)	0.23(10)	0.0(2)
B(Ru) (Å^2)	0.26(18)	=*B*(Pb/Nd)	=*B*(Pb/Nd)	=*B*(Pb/Nd)	=*B*(Pb/Nd)
B(O) (Å^2)	1.0(11)	1.6(10)	1.1(12)	0.8(9)	0.4(10)
R_{wp}	13.44	13.87	16.17	14.94	13.58
R_e	8.25	9.36	8.64	9.80	3.71
R_I	2.54	4.16	3.35	3.21	2.25
			$Pb_{2-x}Gd_xRu_2O_{7-y}$		
Ln content, *x*	1.0	1.2	1.5	1.8	2.0
a (Å)	10.24413(17)	10.23866(14)	10.23298(14)	10.23020(16)	10.2281(2)
x(O1)	0.324(4)	0.327(3)	0.329(3)	0.330(4)	0.332(5)
B(Pb/Gd) (Å^2)	0.50(16)	0.57(13)	0.68(17)	0.6(2)	0.6(3)
B(Ru) (Å^2)	0.6(2)	0.55(18)	0.3(2)	0.3(3)	0.5(3)
B(O) (Å^2)	1.4(13)	1.0(10)	0.5(10)	0.2(11)	1.4(13)
R_{wp}	13.02	11.67	12.44	13.55	13.72
R_e	7.45	7.47	7.92	8.30	8.30
R_I	2.33	1.91	2.33	2.75	2.94

was observed, which is consistent with the XRD data that no vacancy ordering exists in the region $1.0 \leq x \leq 2.0$ in $Pb_{2-x}Nd_xRu_2O_{7-y}$. The structure of $PbNdRu_2O_{7-y}$ was therefore refined with space group $Fd\bar{3}m$ (centrosymmetric setting) using the structural model, Pb and Nd at 16*d* (1/2, 1/2, 1/2), Ru at 16*c* (0, 0, 0), O(1) at 48*f* (*x*, 1/8, 1/8) with $x \approx 0.32$, and O(2) at 8*b* (3/8, 3/8, 3/8). The disordering of Pb and Nd at the 16*d* sites was considered with a constraint that the total occupancy is unity. The site occupation parameters, *g*, of the Ru and O(2) site were also refined. In the final refinement cycle, anisotropic thermal parameters were assigned for all the sites. No correction was made for preferred orientation. Table 1 lists final *R* factors, lattice and structural parameters, and their estimated standard deviations. Table 2 gives interatomic distances and bond angles calculated with ORFFE (17). Figure 7 illustrates the profile fit and difference patterns for $PbNdRu_2O_{7-y}$. The solid line depicts calculated intensities, the overlying dots depict the observed intensities, and Δy_i is the difference between the observed and calculated intensities. Figure 7 shows that the calculated pattern fits the observed one very well.

The occupancy of the O(2) site was determined to be 0.812(8), which is consistent with the results from the synthesis in the evacuated quartz tube that the amount of oxygen vacancy, *y*, is about 0.1. The refinement of the occupancy at the Ru site led to a value of 0.962(4), indicating that the Ru site is almost fully occupied. The occupancy of Pb at the 16*d* site was 0.56(3), leading to a Pb/Nd ratio of 1.27. However, taking into account the

TABLE 4
Selected Interatomic Distances (Å) and Bond Angles (°) for $Pb_{2-x}Ln_xRu_2O_{7-y}$

			$Pb_{2-x}Nd_xRu_2O_{7-y}$		
Ln content, *x*	1.0	1.2	1.5	1.8	2.0
Pb/Nd–O(1)	2.60(3)	2.59(3)	2.58(3)	2.56(3)	2.55(3)
Ru–O(1)	1.958(13)	1.967(13)	1.981(17)	1.990(14)	1.996(16)
Ru–O(1)–Ru	136.7(19)	135.9(19)	134(2)	133.3(19)	133(2)
O(1)–Ru–O(1)	93.0(13)	93.6(13)	94.6(16)	95.4(13)	95.8(10)
	87.0	86.4	85.4	84.6	84.2
			$Pb_{2-x}Gd_xRu_2O_{7-y}$		
Ln content, *x*	1.0	1.2	1.5	1.8	2.0
Pb/Gd–O(1)	2.56(3)	2.53(2)	2.51(2)	2.51(3)	2.50(3)
Ru–O(1)	1.963(16)	1.976(13)	1.983(15)	1.985(17)	1.99(2)
Ru–O(1)–Ru	135(2)	132.7(18)	131.7(19)	131(2)	131(3)
O(1)–Ru–O(1)	94.5(15)	95.8(12)	96.4(12)	96.7(15)	97.2(16)
	85.5	84.2	83.6	83.3	82.8

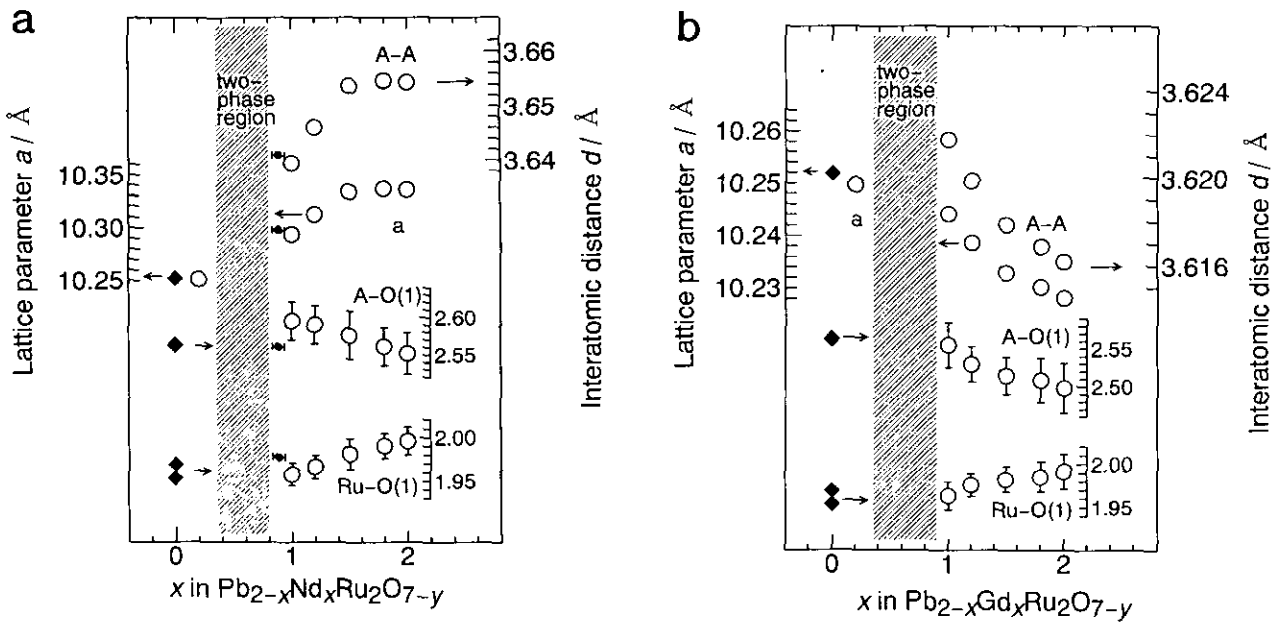

FIG. 8. Composition dependence of the interatomic distances in (a) $Pb_{2-x}Nd_xRu_2O_{7-y}$ and (b) $Pb_{2-x}Gd_xRu_2O_{7-y}$: (○), data obtained by the X-ray diffraction measurements; (●), data obtained by the neutron diffraction measurements; (◆), data for $Pb_2Ru_2O_{6.5}$ taken from Ref. (13).

slightly large standard deviation of the occupancy, the shift from the starting composition might be small.

(b) XRD measurements. Refinements of the structure proceeded with space group $Fd\bar{3}m$ for the lanthanoid-rich region of the solid solutions, $1.0 \leq x \leq 2.0$ in $Pb_{2-x}Ln_xRu_2O_{7-y}$ for both the neodymium and gadolinium systems. The site occupation parameters, g, for Pb/Ln atoms at the 16d site were fixed at the values of the starting compositions. The occupancies of the O(2) site were fixed at the value estimated on the assumption that the oxygen content varies linearly from 7.0 (g = 1.0 at the O(2) site) for $Nd_2Ru_2O_7$ to 6.81 (g = 0.81) for $PbNdRu_2O_{7-y}$. During

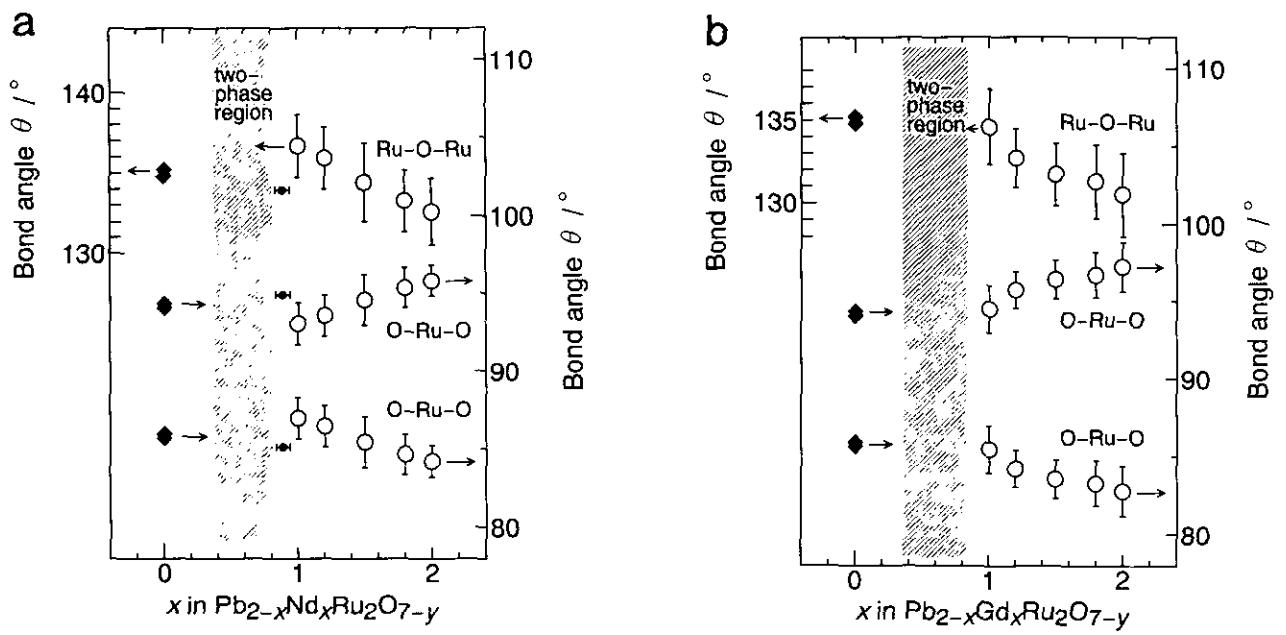

FIG. 9. Composition dependence of the bond angles in (a) $Pb_{2-x}Nd_xRu_2O_{7-y}$ and (b) $Pb_{2-x}Gd_xRu_2O_{7-y}$: (○), data obtained by the X-ray diffraction measurements; (●), data obtained by the neutron diffraction measurements; (◆), data for $Pb_2Ru_2O_{6.5}$ taken from Ref. (13).

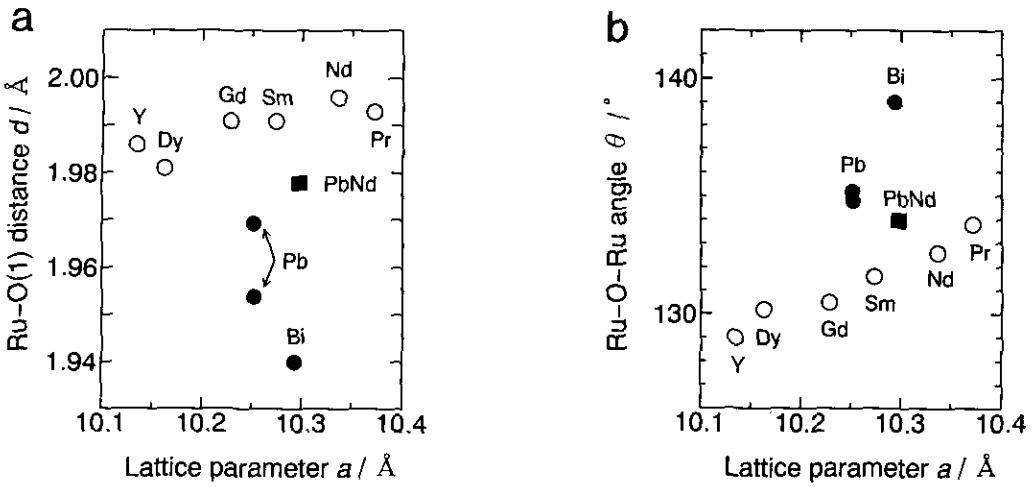

FIG. 10. (a) Ru–O(1) distances and (b) Ru–O–Ru angles in $A_2Ru_2O_{7-y}$ (A = Pb, Bi, rare earth, Y) as a function of lattice parameter. The data for $PbNdRu_2O_{7-y}$ determined by the neutron diffraction measurement are plotted (■). Electrical properties of these compounds are also indicated: (●), metallic; (○), semiconducting.

the latter refinement, when isotropic thermal parameters, B, were refined, the Bs for the O(1) and O(2) sites had to be constrained to the same value; otherwise, the refinements were unstable. The results of refinements for the $Pb_{2-x}Ln_xRu_2O_{7-y}$ system are summarized in Table 3. Table 4 lists interatomic distances and bond angles.

Figures 8 and 9 show, respectively, the composition dependence of the interatomic distances and bond angles in $Pb_{2-x}Ln_xRu_2O_{7-y}$ (Ln = Nd, Gd). No significant change in the lattice parameters was observed in the lead-rich region for the $F\bar{4}3m$ phase. On the other hand, the lattice parameters increase in the neodymium system and decrease in the gadolinium system with increasing x for the lanthanoid-rich region. Despite the difference in the lattice parameter changes between the neodymium and gadolinium systems, similar structural changes were observed in the $Fd\bar{3}m$ phase regions; the A(Pb/Ln)–O(1) distance slightly decreases, the Ru–O(1) distance increases, the Ru–O(1)–Ru angle decreases, and the two O(1)–Ru–O(1) angles split from 90° with increasing x.

The pyrochlore structure consists of a framework of corner-sharing RuO_6 octahedra linked into zigzag chains. The substitution of Ln ions for Pb ions leads to the distortion of RuO_6 octahedra, elongated Ru–O(1) bond lengths, and the reduction of Ru–O(1)–Ru angles, which tends to localize electrons due to reduced Ru–O(1) overlap integrals. The pyrochlore structure is viewed as made up of two networks, $(A_2O)_\infty$ and $(RuO_3)_\infty$, which interpenetrate with each other. The bridging oxide ions, O(1), are connected to both A and Ru ions, and the A—O(1) bond strength might strongly affect the Ru–O(1) bond. These two interactions are competitive; the stronger the A–O(1) bond, the weaker the Ru–O(1) bond. The fact that the A–O(1) distance decreases with the substitution of Ln for Pb indicates the decrease in the Ru–O(1) interaction, being consistent with the change from metallic to semiconducting behavior.

The relationship between the electrical properties and the structures has been reported for the $Bi_{2-x}Ln_xRu_2O_7$ (Ln = Pr–Lu, Y) solid solutions (10, 11). The resistivity increases with x, and a change from metallic to semiconducting behavior is observed between x = 1.2 and 1.4. With increasing Ln^{3+} contents, the lattice parameters in $Bi_{2-x}Ln_xRu_2O_7$ increase for Ln = Pr and Nd and decrease for Ln = Sm and Dy. However, in all the Ln series, the Ru–O(1) bond lengths increase, the distortion of the RuO_6 octahedra increases, and the bend in the RuO_6 zigzag chains increase from x = 0 to 2.0. These structural changes are quite similar to those found in the present study for the $Pb_{2-x}Ln_xRu_2O_{7-y}$ (Ln = Nd, Gd) system.

Figure 10 summarizes the Ru–O(1) bond distances and the Ru–O(1)–Ru angles as a function of lattice parameters for the Ru-containing pyrochlores synthesized previously (10, 11). The metallic region is obviously separated from the semiconducting region; the compounds with Ru–O(1) distances of 1.94–1.97 Å and Ru–O(1)–Ru angles of 134–139° show metallic behavior, and those with Ru–O(1) distances of 1.97–2.00 Å and Ru–O(1)–Ru angles of 129–134° show semiconducting behavior. The bond distance and angle determined by neutron powder diffraction for $PbNdRu_2O_{7-y}$ are 1.9779(4) Å and 133.97(6)°, respectively, which correspond to the borderline between the metallic and semiconducting behavior as shown in Fig. 10.

CONCLUSION

The solid solutions $Pb_{2-x}Ln_xRu_2O_{7-y}$ (Ln = Nd, Gd) have been synthesized from $Pb(NO_3)_2$, $Ln(NO_3)_3 \cdot 6H_2O$, and RuO_2. Two monophasic regions were observed in both the neodymium and gadolinium systems; the oxygen-vacancy-ordered phase with $F\bar{4}3m$ symmetry for the lead-rich region, $0 \leq x \leq 0.2$, and the vacancy-disordered phase with $Fd\bar{3}m$ symmetry for the lanthanoid-rich region, $1.0 \leq x \leq 2.0$. The electrical resistivity measurements showed metallic behavior for the lead-rich region of the solid solution, and a change from metallic to semiconducting in the lanthanoid-rich region around the compositions of x = 1.0–1.2 for the neodymium and x = 1.2–1.5 for the gadolinium systems. Neutron Rietveld analysis of $PbNdRu_2O_{7-y}$ revealed the oxygen nonstoichiometry, y = 0.188, with no vacancy ordering. The X-ray Rietveld analysis for the lanthanoid-rich region revealed that the lattice parameters increase in $Pb_{2-x}Nd_xRu_2O_{7-y}$ and decrease in $Pb_{2-x}Gd_xRu_2O_{7-y}$ from x = 1.0 to x = 2.0. However, similar structural changes were observed in both systems; the Ru–O(1) bond length increases, the bend in the RuO_6 zigzag chain increases, the distortion of the RuO_6 octahedra increases and the A–O(1) bond length decreases with increasing x. These structural changes are similar to those observed for all Ru-containing pyrochlores, $A_2Ru_2O_7$ (A = Pb, Bi, rare earth, Y), and correspond to the metallic-to-semiconducting property changes.

ACKNOWLEDGMENTS

All computations for structure determination were carried out at the Kobe University Information Processing Center. We gratefully acknowledge support from the Tokuyama Science Foundation.

REFERENCES

1. R. J. Bouchard and J. L. Gillson, *Mater. Res. Bull.* **6,** 69, (1971).
2. J. M. Longo, P. M. Raccah, and J. B. Goodenough, *Mater. Res. Bull.* **4,** 191 (1969).
3. R. Aleonard, A. F. Berthand, M. C. Montomry, and R. Pauthenet, *J. Appl. Phys.* **33,** 1205 (1962).
4. A. W. Sleight and R. J. Bouchard, NBS *Spec. Publ.* 364, "Solid State Chemistry, Proceedings of 5th Materials Research Symposium, July 1972," p. 227.
5. H. S. Jarrett, A. W. Sleight, J. F. Weiher, J. L. Gillson, C. G. Frederick, G. A. Jones, R. S. Swingle, D. Swartzfager, J. E. Gulley, and P. C. Hoell, "Valence Instabilities and Related Narrow-Band Phenomena" (R. D. Parks, Ed.), p. 545. Plenum, New York, 1977.
6. J. B. Goodenough, A. Hamnett, and D. Telles, "Localization and Metal–Insulator Transition" (H. Fritzshe and D. Adler, Eds.), p. 161. Plenum, New York, 1985.
7. P. A. Cox, J. B. Goodenough, P. J. Tavener, D. Telles, and R. G. Egdell, *J. Solid State Chem.* **62,** 360 (1986).
8. P. A. Cox, R. G. Egdell, J. B. Goodenough, A. Hamnett, and C. C. Naish, *J. Phys. C* **16,** 6221 (1983).
9. W. Y. Hsu, R. V. Kasowski, T. Miller, and T.-C. Chiang, *Appl. Phys. Lett.* **52,** 792 (1988).
10. R. Kanno, Y. Takeda, T. Yamamoto, Y. Kawamoto, and O. Yamamoto, *J. Solid State Chem.* **102,** 106 (1993).
11. T. Yamamoto, R. Kanno, Y. Takeda, O. Yamamoto, Y. Kawamoto, and M. Takano, *J. Solid State Chem.* **109,** 372 (1994).
12. R. A. Beyerlein, H. S. Horowitz, and J. M. Longo, *J. Solid State Chem.* **72,** 2 (1988).
13. R. A. Beyerlein, H. S. Horowitz, J. M. Longo, M. E. Leonowicz, J. D. Jorgensen, and F. J. Rotella, *J. Solid State Chem.* **51,** 253 (1984).
14. F. Izumi, "The Rietveld Method" (R. A. Young, Ed.) Chap. 13. Oxford Univ. Press, Oxford, 1993.
15. N. Watanabe, H. Asano, H. Iwasa, S. Satoh, H. Murata, K. Karahashi, S. Tomiyoshi, F. Izumi, and K. Inoue, *Jpn. J. Appl. Phys.* **26,** 1164 (1987).
16. F. P. F. van Berkel and D. J. W. Ijdo, *Mater. Res. Bull.* **21,** 1103 (1986).
17. W. R. Busing, K. O. Martin, and H. A. Levy, Report ORNL-TM-306, Oak Ridge National Laboratory, Oak Ridge, TN, 1964.